Thermal Fluid Dynamic Analysis of the MEGAPIE Target Heat Exchanger in Steady State and Transient Conditions

L. Maciocco, L. Sorrentino

CRS4, Centre for Advanced Studies, Research and Development in Sardinia

January 2003

Contents

1   Introduction

The MEGAwatt PIlot Experiment (MEGAPIE) project has the aim to demonstrate the feasibility of a liquid Lead-Bismuth target for spallation facilities at a beam power level of 1 MW [1]. About 650 kW of thermal power has to be removed from the target through a bunch of 12 pin-coolers, using a diathermic oil as secondary coolant. In order to improve the heat exchange in the oil side, a spiral is introduced in the oil riser, which enforces a swirling flow thus increasing the Reynolds number and the heat transfer coefficient.

A single-pin experimental rig was set up and tested in the ENEA-Brasimone facility. A detailed CFD simulation of the experiment was carried out by CRS4, showing the capability of the simulation to give a quantitatively correct prediction of the heat exchange mechanisms in the cooling pin [2].

In order to analyse the performances of the actual Megapie Target Heat eXchanger (THX), the thermal-hydraulic simulation of a sector of the THX, including only one of the 12 pin coolers, has been carried out by CRS4 in steady state and transient conditions, with the assumption of periodical flow-conditions along the THX circumference. The main tasks of this work were the assessment of the global performances of the THX and the evaluation of the thermal field in the solid structure, to be used successively for the calculation of thermal stresses in the target structures.

2   Geometrical Description

The geometry of the Megapie target is continuously evolving, according to the progress in the design studies. The geometry here considered for the upper part of the target was the updated version in June 200. It is shown in Figure 1, where two axial cross sections are shown, one passing through the axis of a pin and one between two adjacent pins.
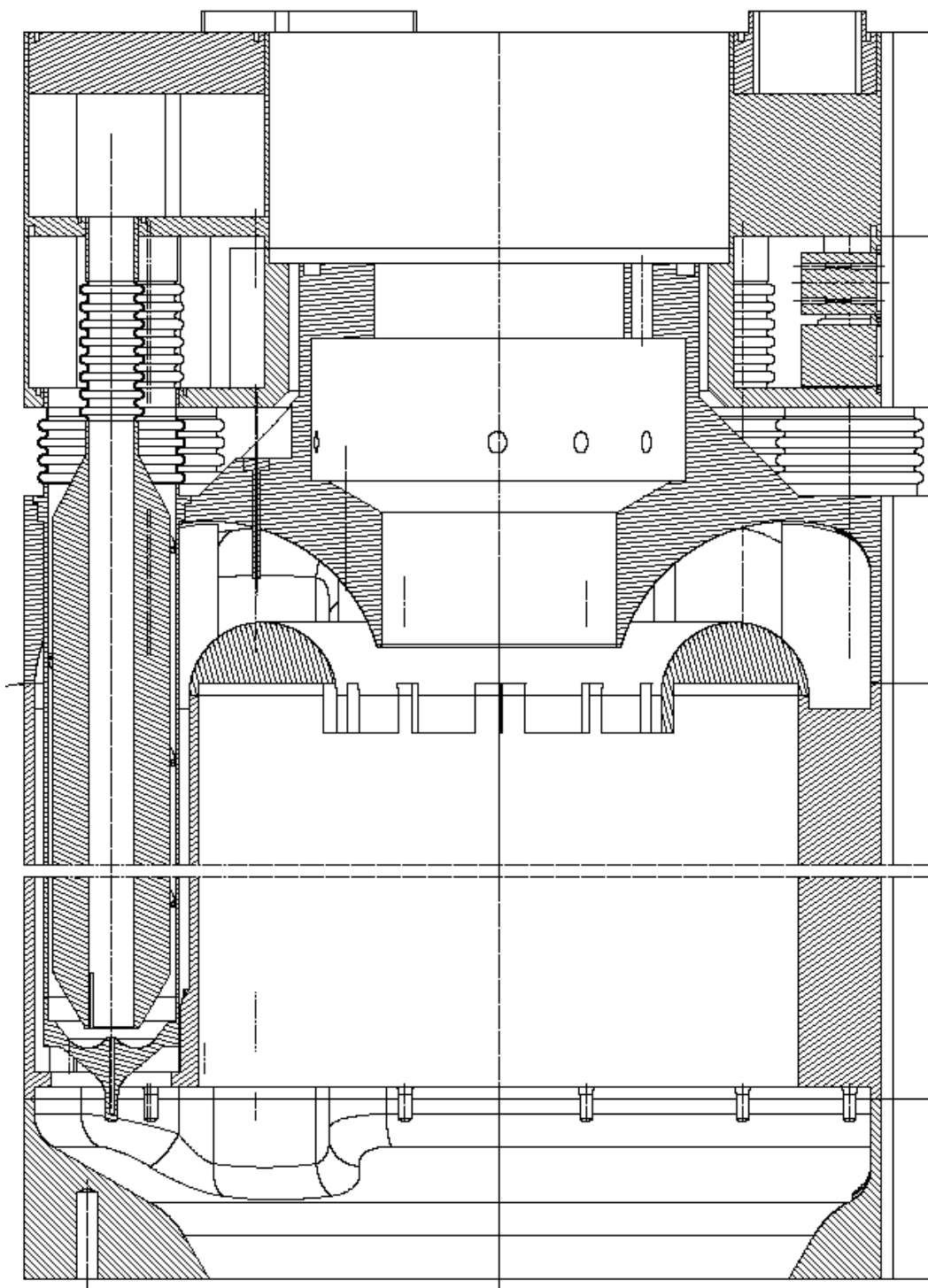
Figure 1 - Description of the THX geometry: two axial cross sections are shown, one passing through the axis of a pin and one between two adjacent pins.

3 Physical Description

The test case consists of a lead-bismuth-eutectic flow incoming in the top part of the THX (coming out from an electromagnetic pump), reversing and flowing around and down along an heat exchanger bayonet pin. This is cooled by an internal flow of synthetic oil (Diphyl THT), coming down in the internal part of the pin and rising along a spiral duct.

The main heat exchanges taking place are those between the PbBi flow and the pin external wall, between the oil flow and the pin internal wall and, less important, the heat transfer across the pin body between the rising and the downcoming oil flow.

The total power exchanged by a single pin is expected to be about 54 kW, corresponding to 650 kW for all the 12 pins of the heat exchanger.

All solid structures are made of AISI 316 steel. The material properties relevant for the simulation are listed in Table 1. Here, the PbBi properties relations as a function of temperature are taken from [3]. The relations for the Diphyl THT oil are the result of polynomial interpolation of data provided by PSI.

The inlet flow characteristics are listed in Table 2. Both the PbBi and oil flow rates correspond to the total nominal flow rates (4 and 10 l/s respectively) divided by 12. However, it should be noted that, for reasons of geometrical symmetry, the considered sector (26°) does not correspond to 1/12 of the full target (30°).

The inlet oil temperature was tuned in order to obtain a total exchanged power as close as possible to the nominal one (650 kW).

Table 1 - Materials properties. The validity range of each formula is reported in brackets.

Property	Lead Bismuth Eutectic (T in ºC)	Diphyl THT (T in ºC)	AISI 316 steel (T in K)
Density [kg/m³]	10737 - 1.375 T (125 ÷ 1000 ºC)	1013.72 - 0.645 T (20 ÷ 370 ºC)	8000
Thermal conductivity [W/ m K]	7.26 + 0.0123 T (125 ÷ 800 ºC)	$0.10963 - 2.574 \times 10^{-5}$ T (20 ÷ 370 ºC)	$15.4767 + 3.448 \times 10^{-3}$ T (273 ÷ 573 K)
Specific heat [J / kg K]	146.5	$1.479 \times 10^{-5} + 3.243$ T $+6.024 \times 10^{-4}$ T^2 (20 ÷ 370 ºC)	520
Molecular viscosity [Pa s]	$3.26 \times 10^{-3} - 6.26 \times 10^{-6}$ T + 4.63×10^{-9} T^2 (150 ÷ 700 ºC)	$2.720 \times 10^{-2} - 5.190 \times 10^{-4}$ T + 4.148×10^{-6} T^2 -1.661×10^{-8} T^3 + 3.289×10^{-11} T^4 - 2.560×10^{-14} T^5 (80 ÷ 370 ºC)	-
Prandtl number	3.06×10^{-2} (at 230 ºC)	16 (at 150 ºC)	-

Table 2 - Flow characteristics

Parameter	Pb-Bi	Oil
Mass flow rate	3.439 Kg/s (×12 = 41.27 Kg/s)	0.733 Kg/s (×12 = 8.78 Kg/s)
Volume flow rate	0.335 l/s (×12 = 4.019 l/s)	0.788 l/s (×12 = 9.461 l/s)
Inlet mean velocity	0.7 m/s	3.111 m/s
Inlet temperature	340 $^{\circ}$C	130 $^{\circ}$C
Inlet turbulence intensity	0.1	0.1
Inlet turbulence length scale	2 mm	2 mm
Reynolds number in the riser	1.6×10^5	4.8×10^4
Reynolds number in the downcomer	2.2×10^4	3.4×10^4

4 Computational Model

The CAD geometry and the computational mesh were built up using the IDEAS software [6]. Star-CD [7] was used to set up the CFD model and to run the simulation.

4.1 Computational domain and mesh

The CAD computational model is illustrated in Figure 2. It consists of a slice of 26° of the full THX, which is a one-pin module. Although the THX has not a real cyclical periodicity (it is symmetrical with respect to an axial plane), this assumption is considered reasonable, at least for those pins which are not beside the real symmetry plane.

A mixed structured-unstructured computational mesh was built, using hexahedral, tetrahedral and prismatic elements. Both integral and arbitrary matching were used to join the various parts of the domain meshed in different ways. A layer of structured hexahedral cells was used in all near-wall regions. The total number of fluid cells is about 330,000, of which about 150,000 are used for the PbBi part. About 140,000 cells were used for the meshing of the solid structures. The total number of cells in the model is about 470,000. Details of the mesh are illustrated in Figure 3, Figure 5 and Figure 6.

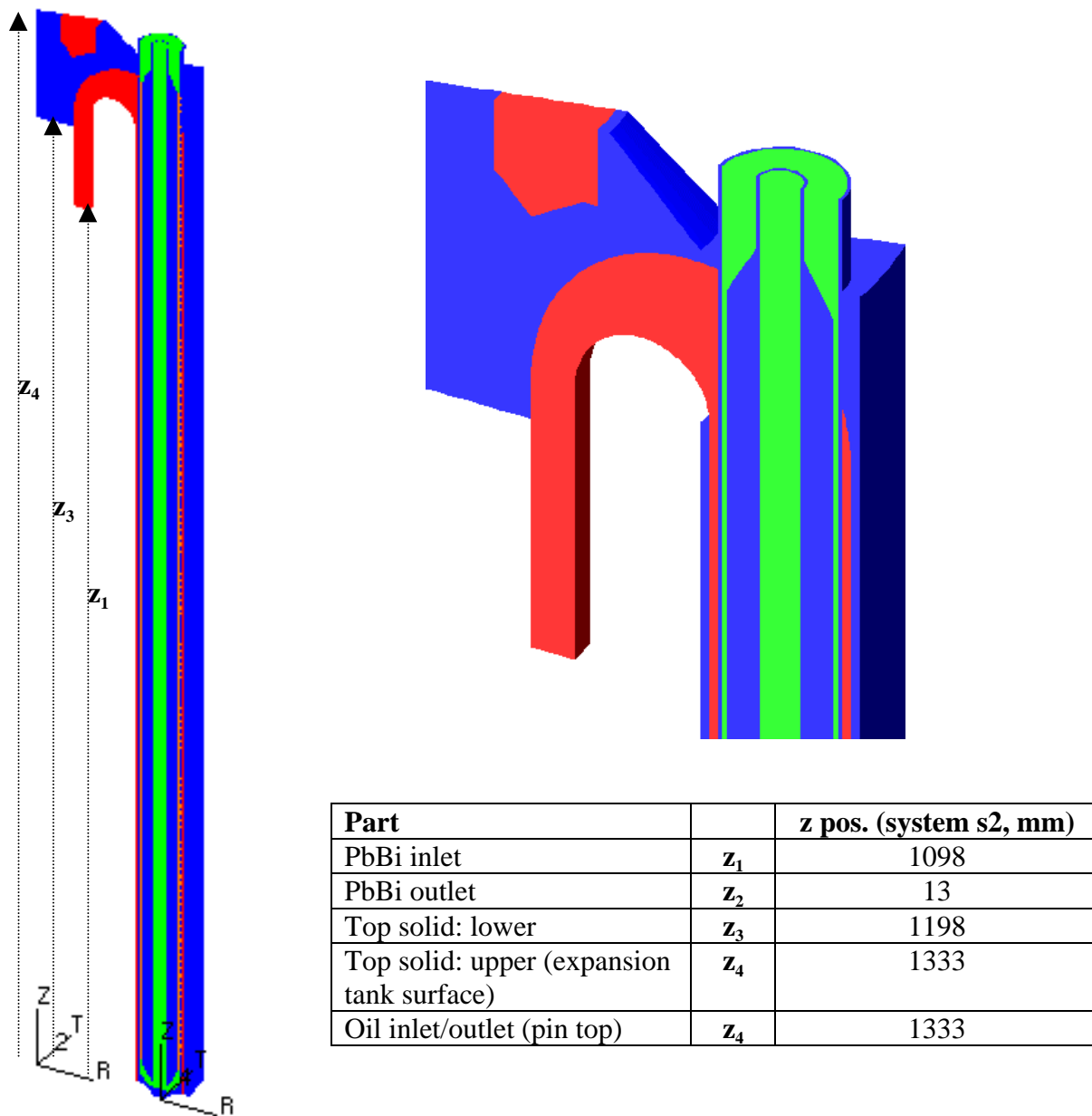| Part		z pos. (system s2, mm)
PbBi inlet	z_1	1098
PbBi outlet	z_2	13
Top solid: lower	z_3	1198
Top solid: upper (expansion tank surface)	z_4	1333
Oil inlet/outlet (pin top)	z_4	1333

Figure 2 - Computational model: full model (left) and top part, with and without pin (right). The PbBi is coloured in red, the oil in green and the steel in blue. The two cylindrical reference systems s2 and s4, located at the height of the lowest point of the pin on the target axis and on the pin axis respectively, are shown.
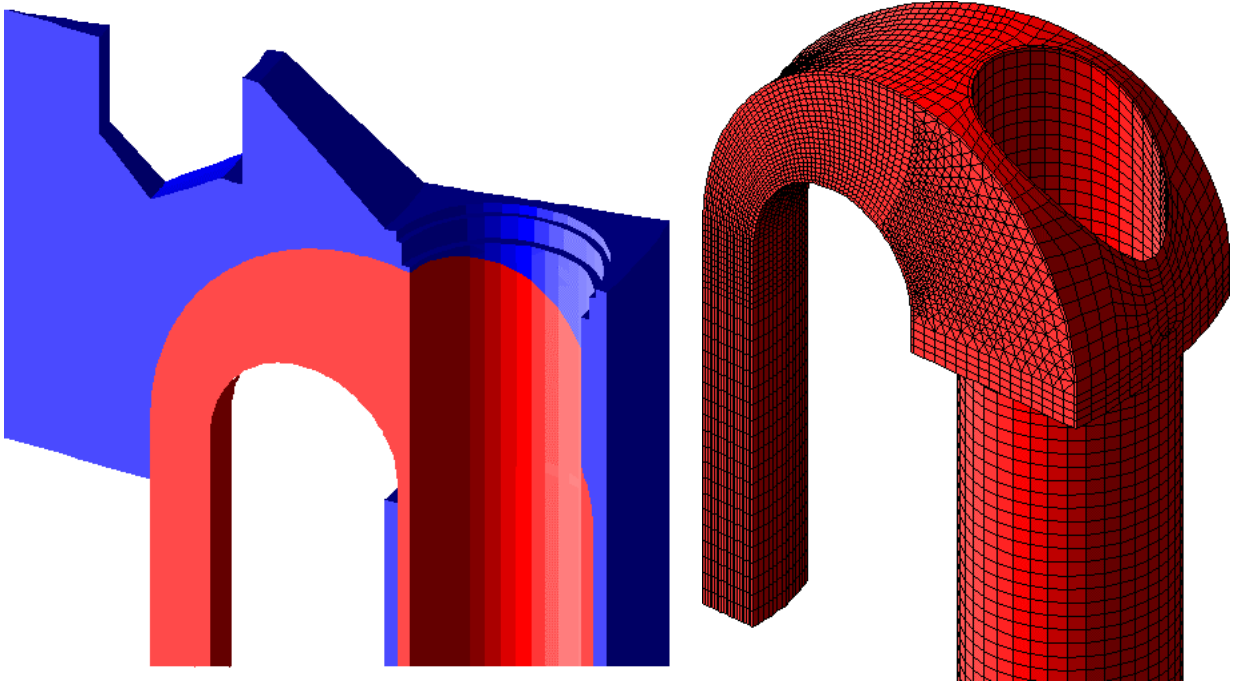
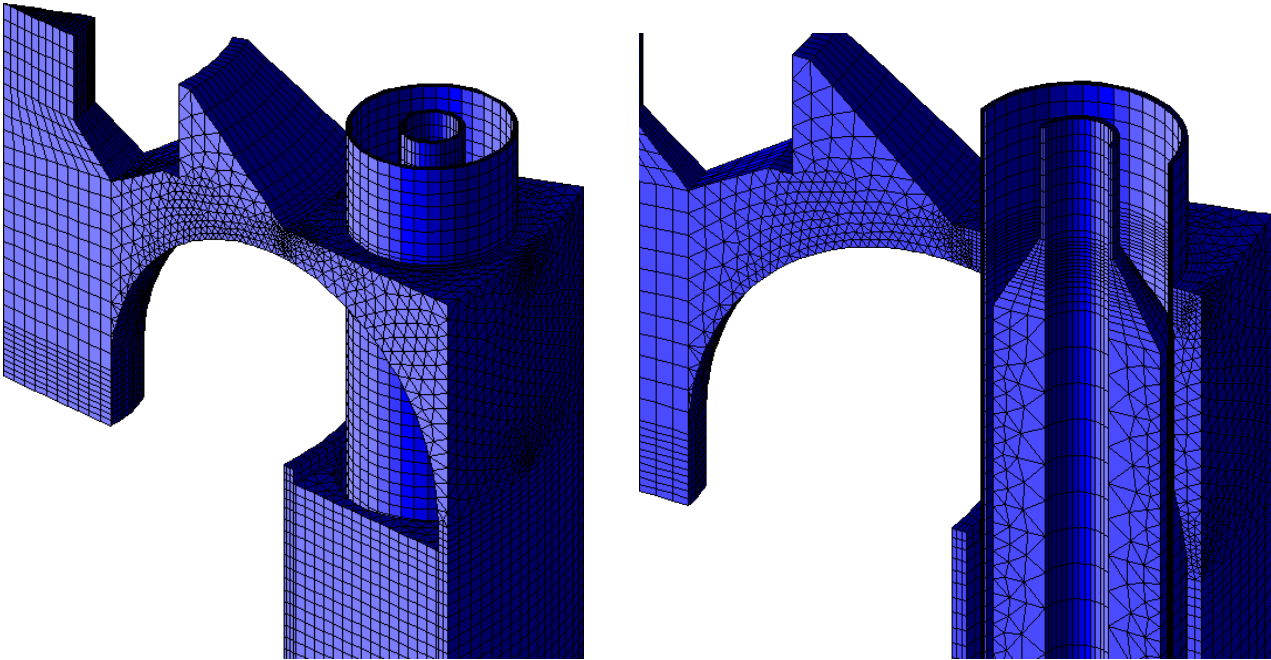Figure 3 - Computational mesh: top part, half-domain without pin (left) and LBE (right).

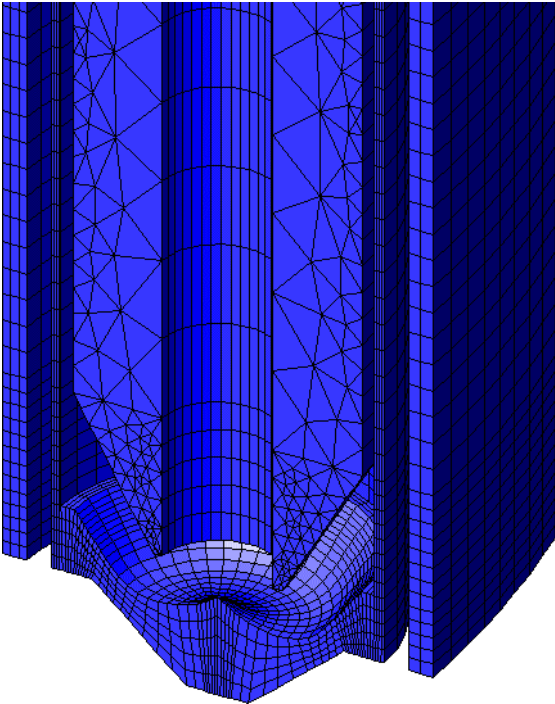Figure 4 - Computational mesh: solid structures of the top part of the target.

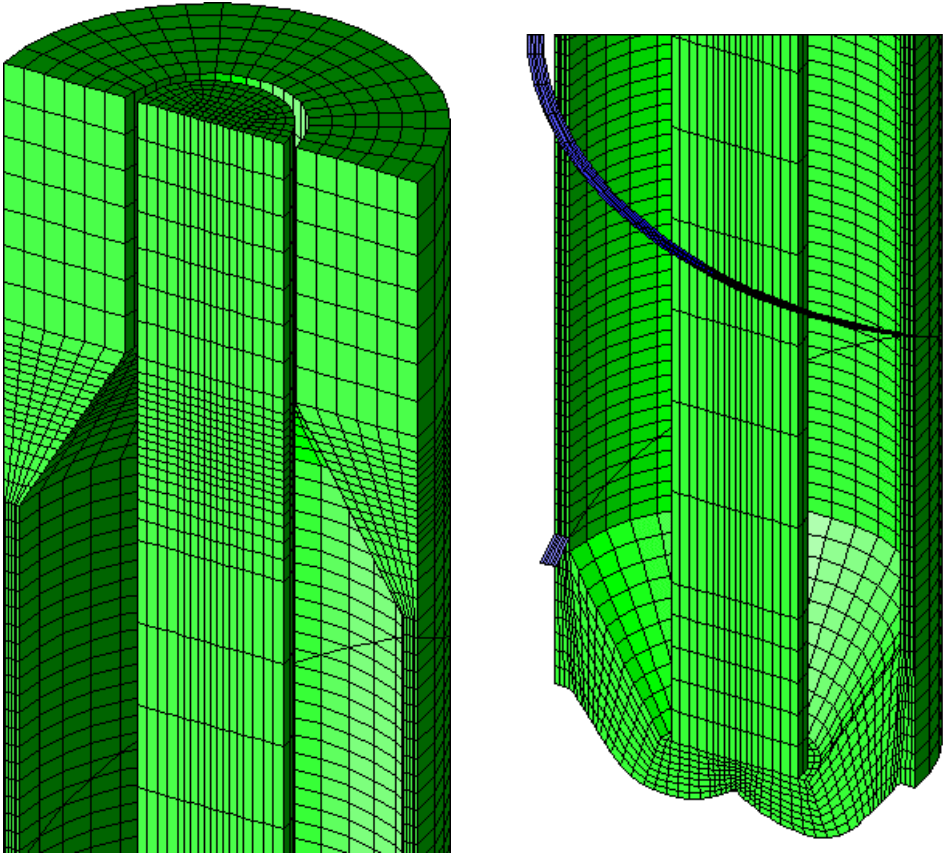Figure 5 - Computational mesh: solid structures of the bottom part of the target.

Figure 6 - Computational mesh: top and bottom part of the oil part with the spiral wire (in blue).

4.2   Numerical schemes

Steady-state calculations were performed using the SIMPLE integration algorithm [7]. The following convection schemes were used:

- momentum equations: MARS;

- enthalpy equation: MARS;

- turbulence equations: MARS.

The PISO algorithm was used for the transient calculation.

4.3   Turbulence modelling

A Chen k-ε model with Wall Functions [7] was used for all the test cases performed.

Star-CD Wall-Functions have been modified through user programming, in order to take into account the effect of the low Prandtl number of the Pb-Bi [9]. In particular, a dynamic switching from linear to logarithmic thermal boundary layer y_T^+ has been implemented as the larger root of the implicit equation [8]

$$\frac{Pr_t}{\kappa} \log(E_T \, y_T^+) = Pr \, y_T^+ \tag{1}$$

where κ=0.42, $Pr_t = 0.9$ and E_T is deduced from the following formula [8]

$$E_T = \exp\left\{9\kappa\left[\left(\frac{Pr}{Pr_t}\right)^{0.75} - 1\right]\left[1 + 0.28\exp\left(-0.007\frac{Pr}{Pr_t}\right)\right]\right\} \tag{2}$$

The resulting value of y_T^+ depends on the value of the molecular Prandtl number, which depends on temperature according to Table 1. As a result, y_T^+ grows with temperature. At a PbBi temperature of about 170 ºC (which is the minimum temperature in a steady-state run), its value is about 350. Therefore, being the maximum value y^+ in the domain where Wall Functions are applied about 150 (see Figure 8), the linear law (pure conduction) is always used for thermal wall functions.

4.3.1   Turbulent Prandtl number

In two-equation turbulence models turbulent heat fluxes are modelled using a gradient-diffusion approach, where the turbulent heat diffusion coefficient α_t is set proportional to the turbulent cinematic viscosity ν_t through the turbulent Prandtl number

$$\alpha_t = \nu_t \, / \, Pr_t$$

The turbulent Prandtl number is usually considered constant and set to a standard value of 0.9. However, this approach could be unsuitable for liquid-metal flows, due to their very low molecular Prandtl number [10] [4].

In order to estimate the influence of the low Pr on the turbulent heat exchange, the following expression for Pr_t as a function of Pr and the turbulent Reynolds number Re_t has been deduced from [11]:

$$Pr_t = c_1 + \frac{c_2}{Pr \, Re_t} \tag{3}$$

where $c_1 = 0.9$, $c_2 = 0.0899$ and

$$Re_t = c_\mu^{-0.25} \frac{\nu_t}{\nu}.$$

Eq. (3) has been implemented in the CFD model.

4.4 Boundary conditions

4.4.1 Inlet/Outlet

Inlet and outlet boundary conditions are applied as illustrated in Figure 7. Uniform velocity and temperature profiles were used both for the PbBi and for the oil inlets, with velocity magnitudes and temperatures as reported in Table 2. Constant inlet turbulence characteristics were also considered. Although inlet distributions have a minor influence on the oil side, the flow pattern of the PbBi flow in the top bend could be influenced by velocity and turbulence distributions. However, lacking at the moment any precise information about the characteristics of the flow coming out from the electromagnetic pump, a turbulence intensity of 0.1 and a turbulence length scale of 2 mm were assumed.

A mass-flow preserving boundary condition [7] was applied on the flow outlet.

4.4.2 External walls

All external walls are considered adiabatic, apart from the pin-cap bottom wall (Figure 7). Here, the heat exchange with the PbBi in the flow collector at the exit of the downcomer is modelled by applying a constant temperature equal to the PbBi outlet temperature, with a heat resistance corresponding to a heat exchange coefficient of 10^4 W/m^2/K, which is typical for this PbBi flow configuration [5].

4.4.3 Fluid-solid interfaces

All fluid solid interfaces are considered as conductive walls with zero thermal resistance, apart from the spiral baffle, where a thermal resistance corresponding to the real thickness of the spiral wire (considered made of AISI 316) was applied (1.093×10^{-4} m^2 K/W).

Wall-Functions are used on all the wall boundaries. Figure 8 shows the typical distributions of y^+ in the PbBi and Diphyl wall boundaries. It can be seen that the range of y^+ is within the logarithmic layer ($11 < y^+ < 300$) everywhere but in a small region at the beginning of the oil riser, where a flow recirculation takes place (see Sec. 6.1)

4.4.4 Cyclic boundaries

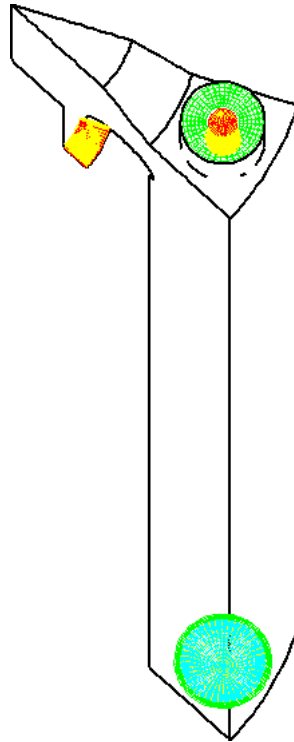Cyclic conditions are applied on the side surfaces of the model.

Figure 7 - Inlet (red-yellow) and outlet (green) boundary conditions. The wall boundary condition on the pin-cap bottom surface is also shown in cyan.
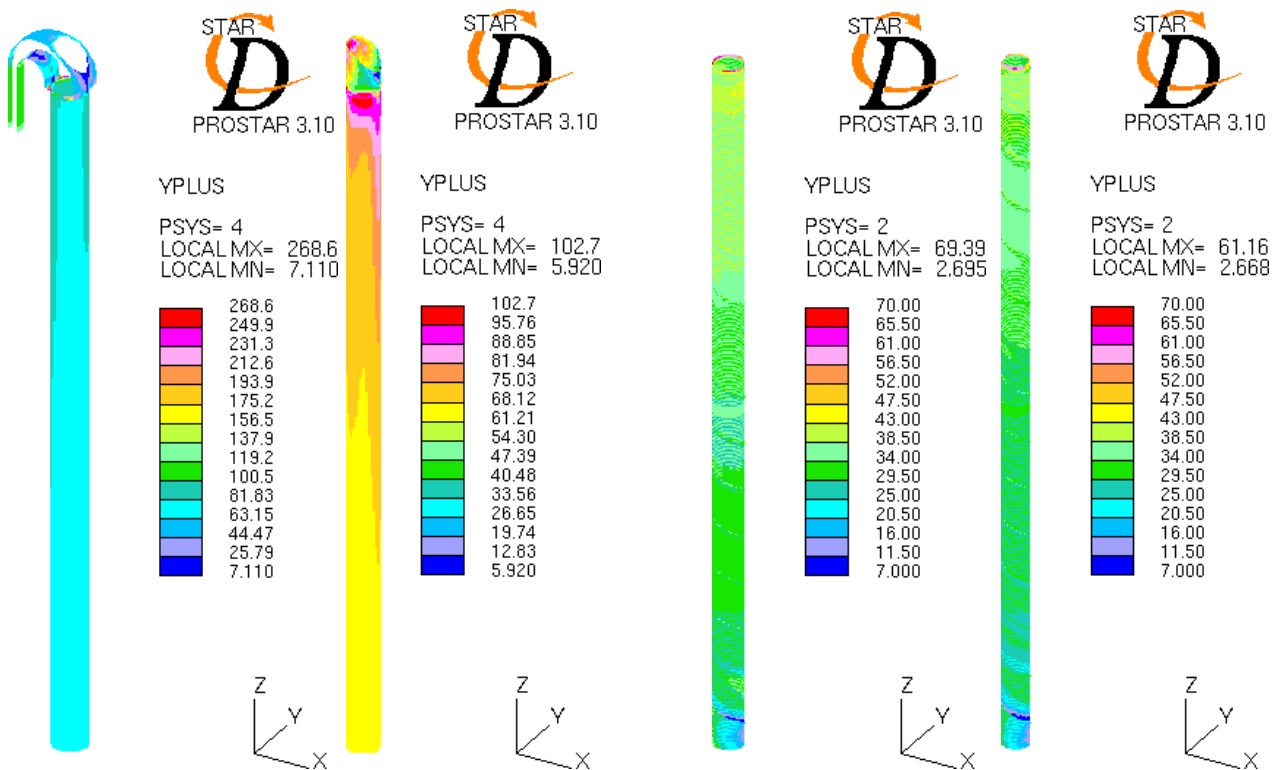

Figure 8 - Typical distribution of y^+ in the Pb-Bi (first two figures on the left) and in the oil riser (on the right) walls.
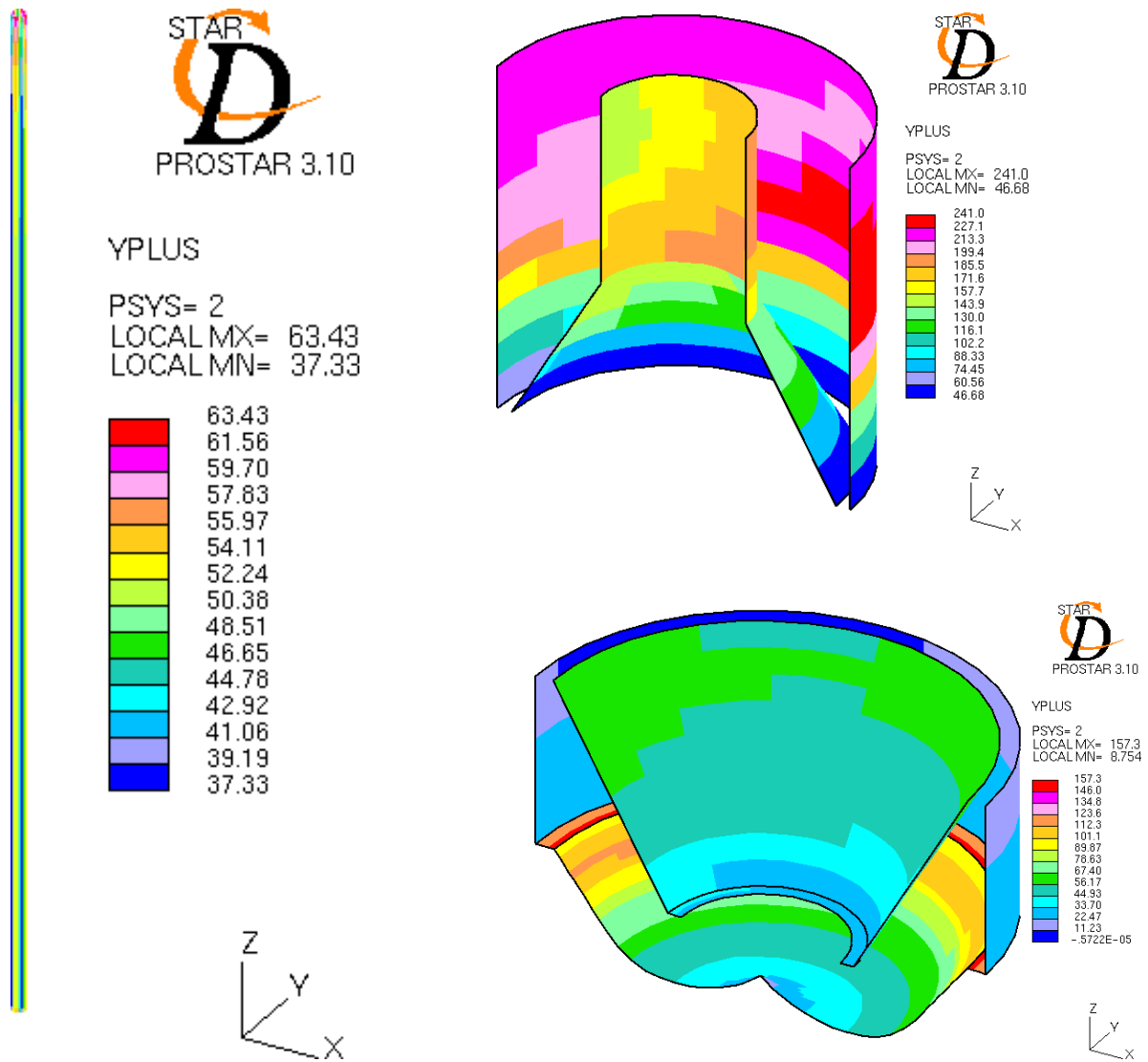
Figure 9 - Typical distribution of y^+ in the oil downcomer (left) and in the reversing and collector (right) walls.

5   List of Test Cases

Four calculations has been carried out, three in steady state conditions and one simulating a beam shut-down transient (Table 3). Concerning steady-state simulations, three different inlet velocity profiles were considered, one uniform and two tilted, in order to study the effect of the characteristics of the incoming flow on the flow behaviour in the reversing bend, and therefore on the temperature distribution in the upper part of the pin.

One transient calculation was carried out starting from the results of case s1 and applying a time-varying inlet temperature simulating the effect of a beam shut down (see Sec. 7).

Table 3 - List of test cases: w is the inlet normal velocity components, r_1 and r_2 are the minimum and maximum radia of the inlet annular channel respectively.

Case	Time dependence	Inlet normal velocity profile
s1	steady state	uniform
s2	steady state	tilted (higher at $r=r_1$): $$w(r) = \overline{w} + 1.88 \times 10^{-2}\left(\frac{1}{r} - \frac{2}{r_1 + r_2}\right)$$
s3	steady state	tilted (higher at $r=r_2$): $$w(r) = \overline{w} - 2.658 \times 10^{-2}\left(\frac{1}{r} - \frac{2}{r_1 + r_2}\right)$$
t1	transient	uniform

6 Steady-state analysis (cases s1, s2 and s3)

6.1 Simulation with uniform inlet velocity profile (case s1)

A satisfactory convergence was obtained, as shown in Figure 10. The global results of the simulation are reported in Table 4. It can be seen that the heat exchanged is about 695 kW, slightly higher than the one expected (650 kW). The corresponding global heat exchange coefficient H_c can be calculated as

$$H_c = \frac{W}{\overline{\Delta T}\, S}$$

where

$$\overline{\Delta T} = \frac{\Delta T_a - \Delta T_b}{\ln(\Delta T_a / \Delta T_b)}$$

is the mean logarithmic temperature difference, being $\Delta T_a = T_{LBE,in} - T_{oil\_out}$ and $\Delta T_b = T_{LBE,out} - T_{oil,in}$, and S the heat exchange surface (0.213 m^2). According to data in Table 4, it results $H_c \approx 25000$ W/m^2/°C. The distribution of the mean heat exchange coefficient along the LBE downcomer is shown in Figure 11. A much higher value (up to about 40 %) can be observed in the first part of the downcomer, likely due to the high turbulence level of the flow coming from the bend and entering the downcomer. This could explain the higher value of H_c with respect to the one expected.

The estimated total-pressure difference in the LBE side is about 4000 Pa. Friction losses have been calculated by adding to this value the estimated pressure difference generated by buoyancy effects, yielding a total value of friction losses of about 6500 Pa. A rough estimation of the friction losses in the bend is also given (an outlet section where to estimate a mean total pressure can not be easily identified). A total-pressure drop of 275 kPa was calculated in the oil side.

Concerning power balances, it can be seen that the sum of the heat fluxes in the LBE side (across the pin wall and across the top wall) is 57994 W, coherently with the sum of the heat fluxes in the oil side (across the pin wall, across the pin cap minus the power entering the system through the pin bottom), which yields 57920 W. The little difference in the enthalpy fluxes is partially due to the power entering the system from the pin bottom and partially to the fact that they are evaluated with a mass-weighted average.

Some velocity and temperature field extrema are reported in Table 5.

The LBE velocity field in the bend is shown in Figure 12. A large flow-detachment area can be observed in the internal part of the bend. A stagnation region is also formed behind the pin near the top wall. The corresponding fields of piezometric (computed) and static (piezometric plus hydrostatic, computed with the reference value of the density at T = 340 ºC) pressure are plotted in Figure 13. Pressure values are relative to the highest cell in the PbBi computational domain, corresponding approximately to the point where the expansion tank should be connected. In order to get absolute values of the static pressure, the hydrostatic head of the expansion container plus the gas pressure at the free surface should be added to the values in Figure 13.

The oil velocity field in the top and bottom end of the pin are plotted in an axial section in Figure 14, together with the flow pattern in the first part of the spiral duct. A recirculation region can be observed in the annular duct reversing the downcoming flow towards the spiral riser. A large stagnation area is also formed in the first part of the spiral duct, making the oil velocity rise to a maximum of 8.3 m/s. The swirling flow becomes uniform after a couple of spiral pitches.

The resulting PbBi temperature field in the upper part of the target is shown in Figure 15. Due to the stagnating flow, an area at low temperature (about 245 ºC) is generated behind the pin, causing a highly non-uniform temperature field in the top part of the target. This is also shown in Figure 16, where the temperature distribution in the whole PbBi domain and in the target solid structures is plotted. A detail of the temperature field in the flange where the cooling pin is connected to the target structure is shown in Figure 17. This is the part where the highest thermal stresses are expected.

Figure 18 shows the temperature field in all the pin surfaces, starting form the external wall of the pin pipe to the internal wall of the pin body. The strong temperature gradients generated in the upper region can be also observed in Figure 19, where the temperatures in the upper and lower parts of the pin are plotted. A zone at higher temperature is generated in the lower part of the pin by the recirculation region in the first part of the spiral (Figure 14).

6.2   Simulation with tilted inlet velocity profile (cases s2 and s3)

Converge levels analogous to the one obtained for case s1 (Figure 10) were obtained for cases s2 and s3.

The PbBi velocity fields in the bend obtained in the two cases with tilted velocity profiles are shown in Figure 20 and Figure 21. It can be seen that the flow field for case s2 (higher inlet velocity closer to the target axis) is equivalent to the one obtained case s1, with a flow detachment in the internal part of the bend. In case s3 the flow pattern in the bend changes completely, with the flow detachment taking place in the external part of the bend. The resulting pressure field for case s3 is shown in Figure 22; the influence of dynamic pressure on the static pressure field is again very low. Some differences can be noticed in the temperature distribution in the PbBi and in the top target structures, as shown in Figure 23 and Figure 24. Slight lower temperature gradients can be observed in the target structures.

As expected, the global performances of the THX are independent of the inlet profile characteristics, as it can be deduced from Table 4.

6.3   Tables and figures

Table 4 - Global results for steady-state simulations (quantities in brackets are referred to 12 pins).

Quantity	Case s1	Case s2	Case s3
PbBi outlet mean normal velocity	0.457 m/s	0.457 m/s	0.457 m/s
PbBi outlet mean temperature	226 ^{o}C	226 ^{o}C	226 ^{o}C
PbBi inlet-outlet mean temperature diff.	114 ^{o}C	114 ^{o}C	114 ^{o}C
PbBi inlet-outlet total-pressure difference (dp_{io})	4132 Pa	4325 Pa	4731 Pa
PbBi: estimated buoyancy pressure $\rho\beta g\Delta T_{io}\ \Delta z_{io}$ ($\rho\beta$ = 1.375 Kg/m^3 ^{o}C) (dp_b)	1845 Pa	1845 Pa	1845 Pa
PbBi: estimated friction losses in the target (dp_{io} + dp_b)	6479 Pa	6170 Pa	6576 Pa
PbBi: estimated friction losses in the bend	480 Pa	537 Pa	659 Pa
PbBi inlet-outlet enthalpy flux difference (mass flow rate average)	-57924 W (-695.1 kW)	- 58045 W (-696.5 kW)	-57741 W (-692.9 kW)
PbBi: power exchanged with the top wall	-428 W	-441 W	-387 W
PbBi: power exchanged with the pin wall	-57566 W	-57657 W	-57537 W
Oil outlet mean normal velocity	0.467 m/s	0.467 m/s	0.467 m/s
Oil outlet maximum velocity	4.30 m/s	4.30 m/s	4.30 m/s
Oil outlet mean temperature	170 ^{o}C	170 ^{o}C	170 ^{o}C
Oil inlet-outlet mean temperature diff.	40 ^{o}C	40 ^{o}C	40 ^{o}C
Oil temperature at the downcomer outlet	131 ^{o}C	131 ^{o}C	131 ^{o}C
Oil inlet-outlet total pressure difference	275 kPa	275 kPa	275 kPa
Oil inlet-outlet enthalpy flux difference (mass flow rate average)	58315 W (699.8 kW)	58437 W (701.2 kW)	58153 W (697.8 kW)
Oil: power exchanged with the pin wall	57375 W	57491 W	57212 W
Oil: power exchanged with pin-cap wall	749 W	749 W	749 W
Oil: power exchanged across the pin body	1024 W	1024 W	1024 W
Power entering the system from the pin-cap bottom wall	204 W	204 W	204 W

Table 5 - Maximum temperatures and velocities with their location. Co-ordinates are referred to the reference systems s2 and s4 shown in Figure 2. Values are selected among cell data.

Quantity	Case s1 (position r,θ,z [mm,deg,mm])	Case s2 (position r,θ,z [mm,deg,mm])	Case s3 (position r,θ,z [mm,deg,mm])
Max PbBi velocity	0.778 m/s (s2: 63, 0, 1223)	0.769 m/s (s2: 46, 0, 1100)	0.823 m/s (s2: 63, 0, 1223)
Min PbBi temperature	215 ºC (s2: 130, 0, 39)	215 ºC (s2: 132, 0, 39)	216 ºC (s2: 182, 0, 22)
Max Oil velocity	8.318 m/s (s4: 130, 0, 80)	8.318 m/s (s4: 130, 0, 80)	8.318 m/s (s4: 130, 0, 80)
Max Oil temperature	176 ºC (s4: 25, 1, 1259)	176 ºC (s4: 25, 1, 1259)	176 ºC (s4: 25, 1, 1259)
Max pin-wall ext. surf. temp.	318 ºC (s4: 27, -3, 1270)	318 ºC (s4: 128, -3, 1270)	318 ºC (s4: 128, 0, 1256)
Max pin-wall int. surf. temp.	283 ºC (s4: 25, 3, 1269)	283 ºC (s4: 25, 3, 1269)	282 ºC (s4: 25, 3, 1265)
Max pin-body ext. surf. temp.	168 ºC (s4: 23, 0, 1278)	168 ºC (s4: 23, 0, 1278)	168 ºC (s4: 23, 0, 1278)
Max pin-body int. surf. temp.	151 ºC (s4: 9, -3, 1299)	151 ºC (s4: 9, -3, 1299)	151 ºC (s4: 9, -3, 1299)
Max pin-cap temperature	221 ºC (s4: 5, 1, 1)	221 ºC (s4: 5, 1, 1)	221 ºC (s4: 5, 1, 1)
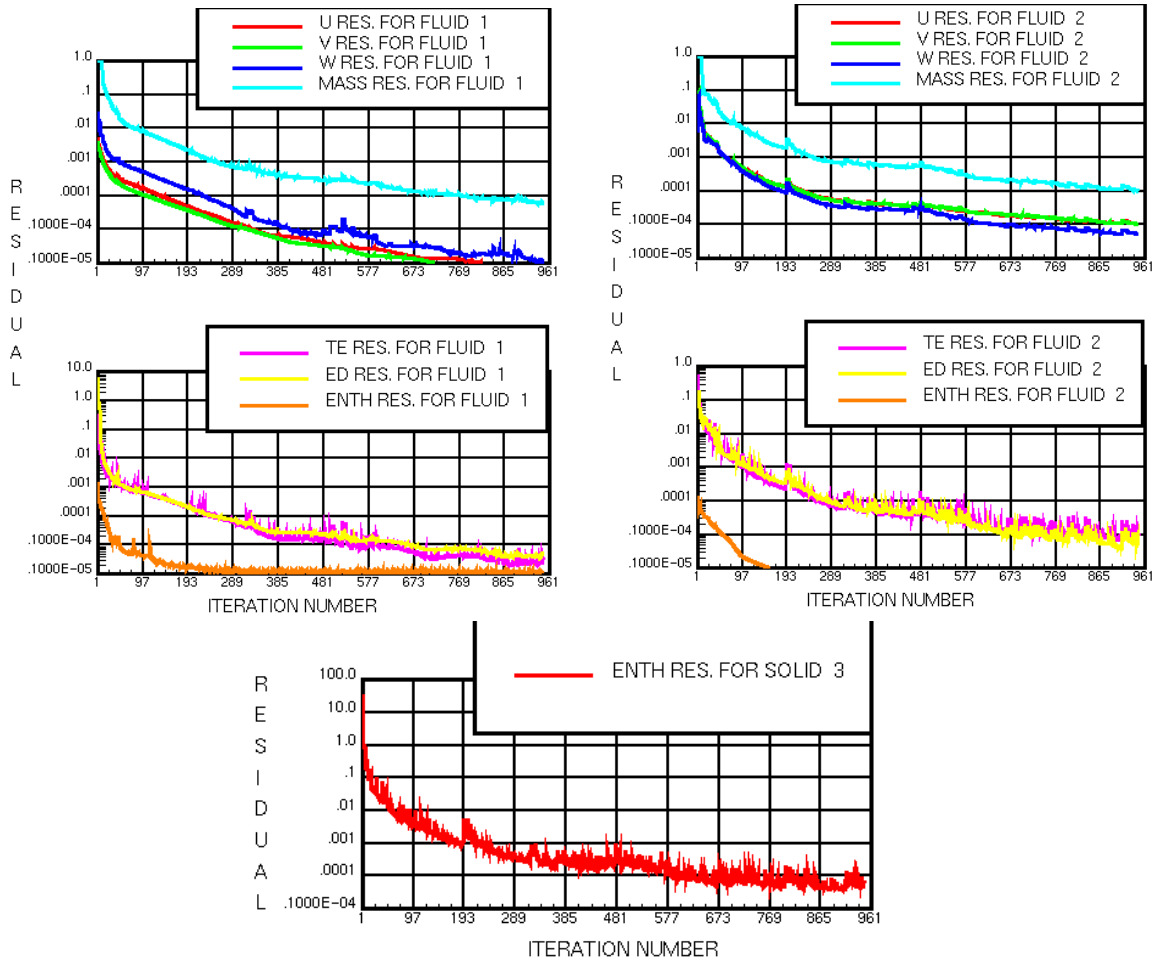
Figure 10 - Case s1: residuals history for the PbBi (top-left), in the oil (top-right) and in the steel (bottom).
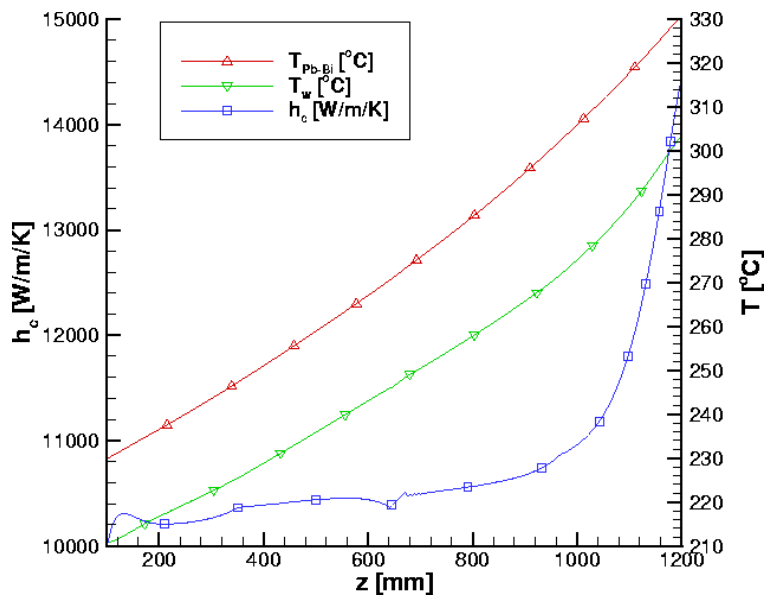
Figure 11 - Case s1: mean heat exchange coefficient and mean wall and fluid temperatures along the Pb-Bi downcomer.

17
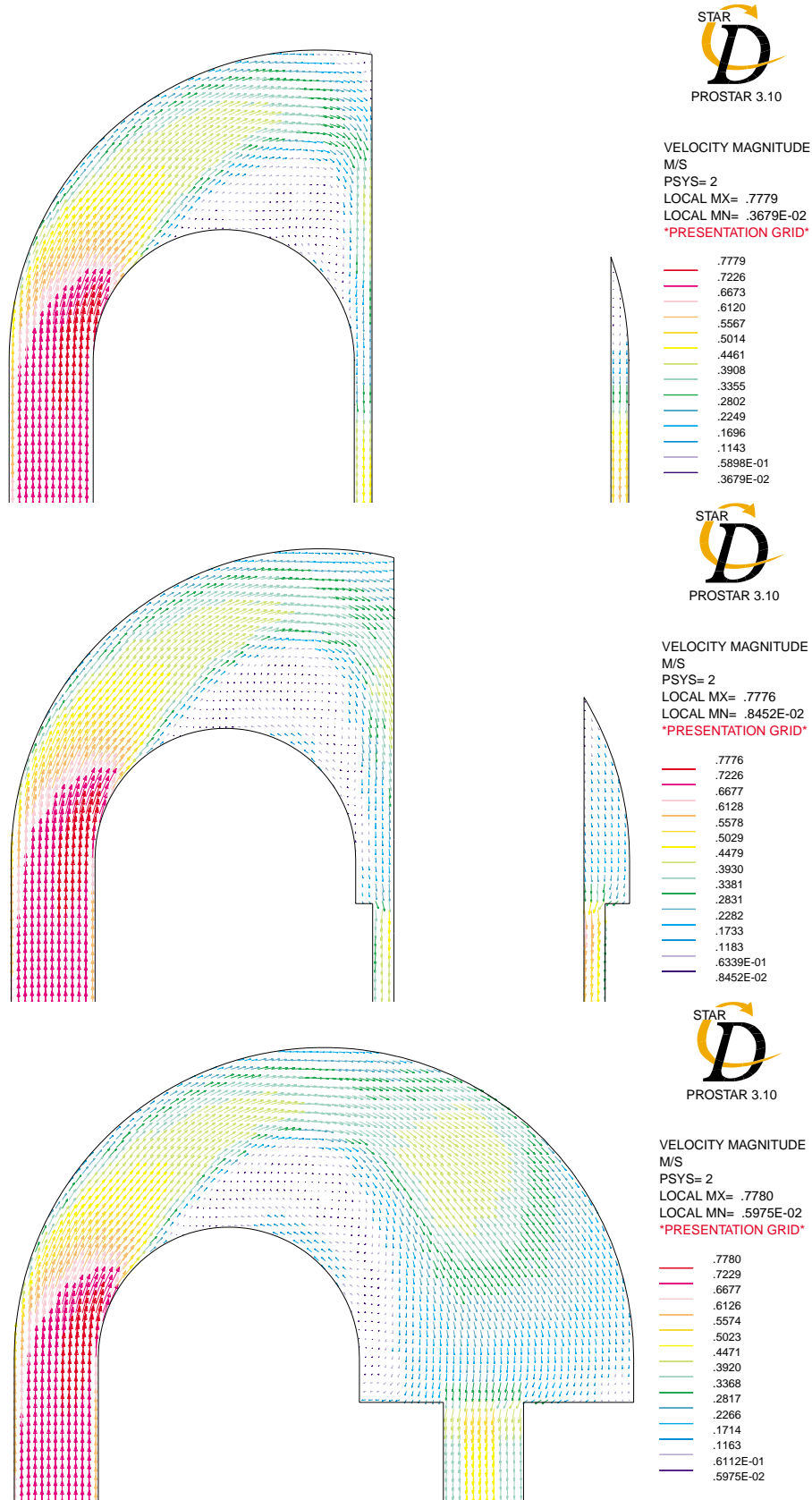
Figure 12 - Case s1: PbBi velocity field in various rz sections (system s2) cutting the top part of the target. From top to bottom: θ = 0, 6, 11 deg.
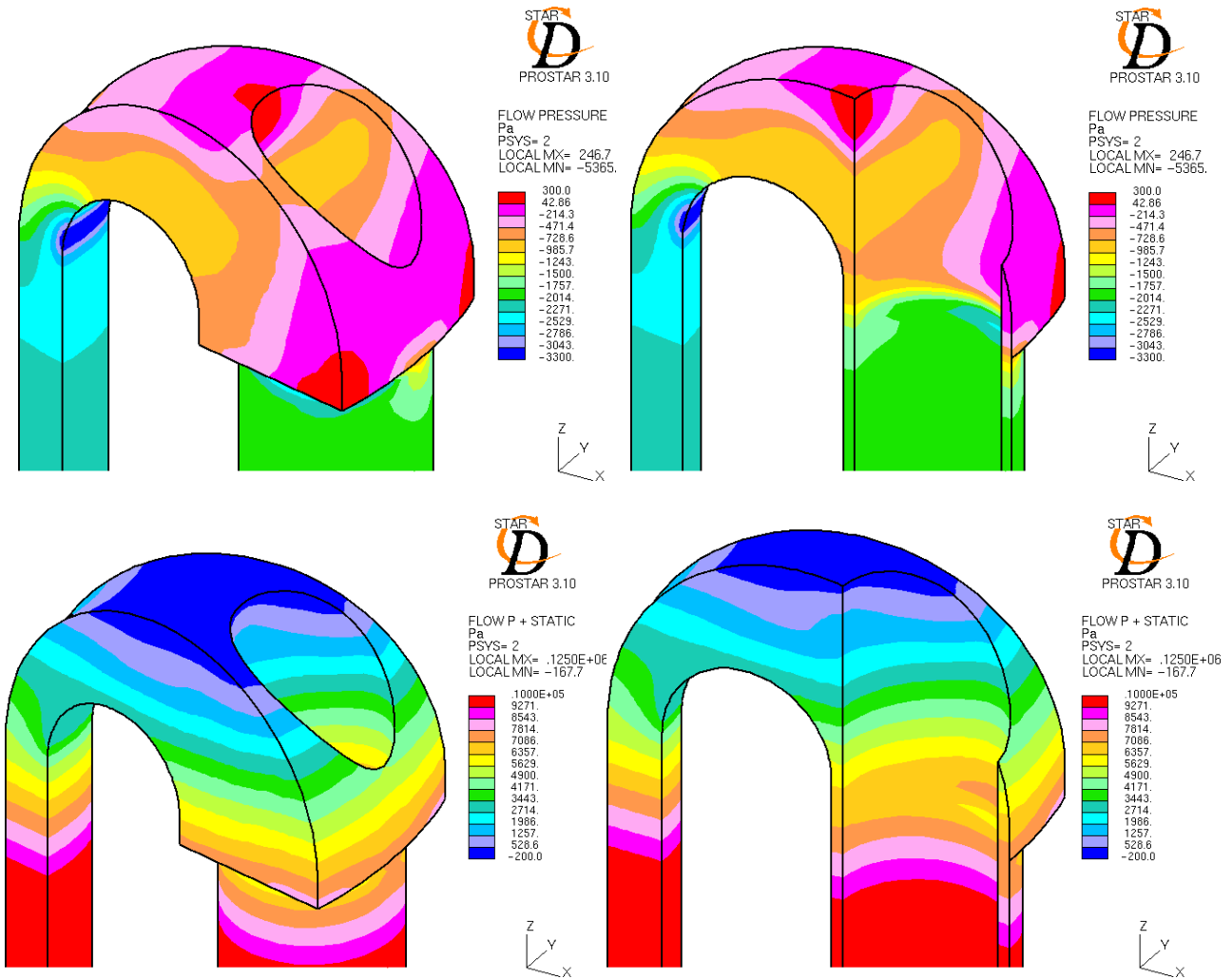
Figure 13 - Case s1: PbBi pressure field in the top part of target. The piezometric pressure (top) and the static pressure (bottom) relative to the highest PbBi cell are plotted on the full and on the halh model. The absolute pressure values can be obtained by adding the static head of the expansion container. Data are averaged on model vertices.
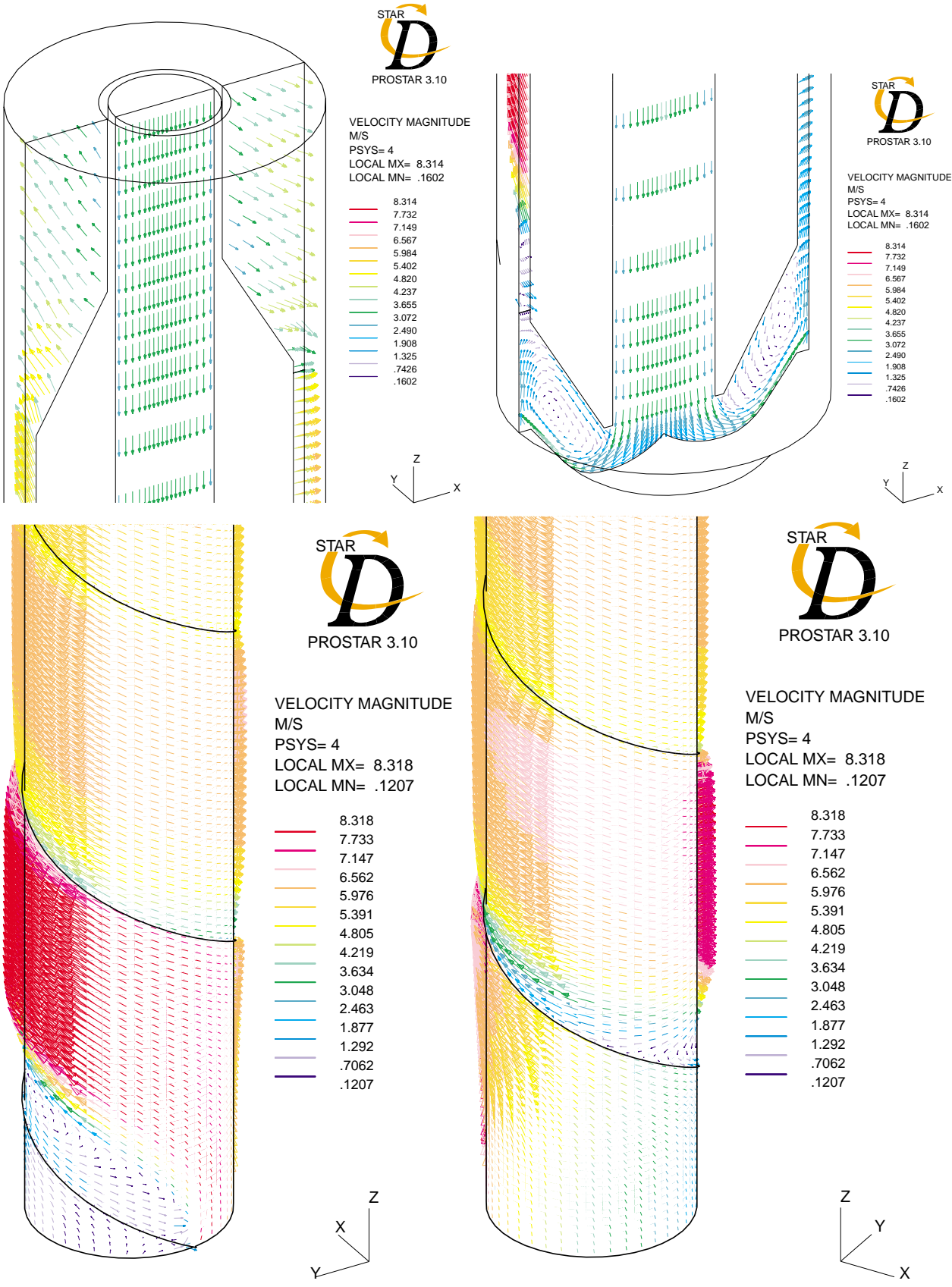
Figure 14 - Case s1: oil velocity field in the top and bottom parts (left) and within the first part of the spiral duct, where a flow recirculation occurs (right).
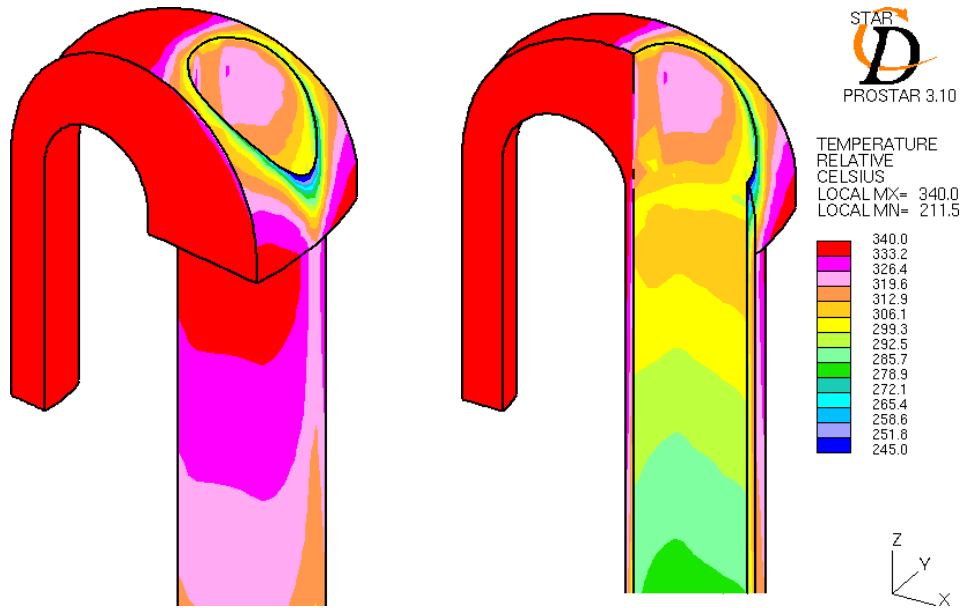
Figure 15 - Case s1: PbBi temperature field in the top part of the target; full and half model. Data are averaged on model vertices.
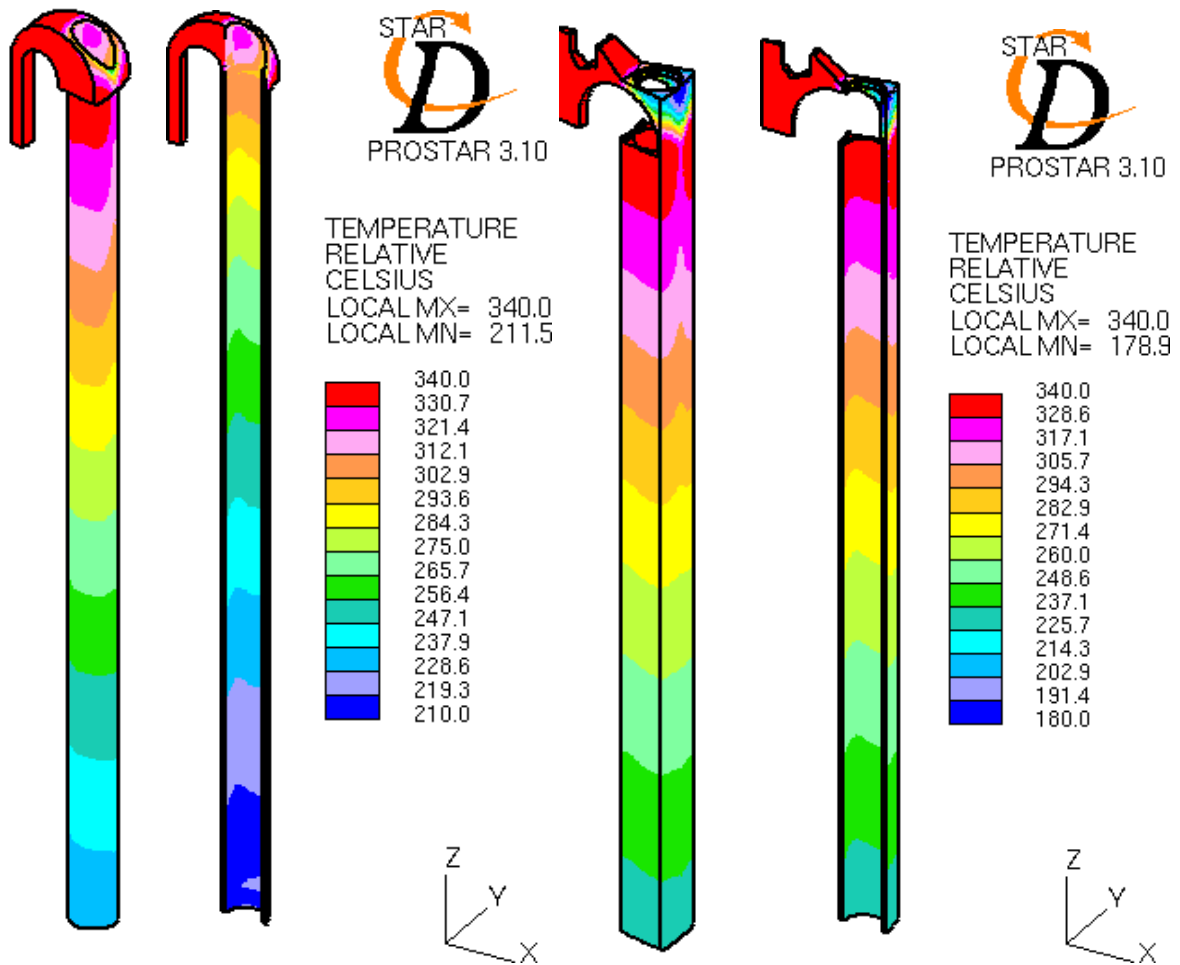
Figure 16 - Case s1: temperature field in the PbBi (left) and in the target solid structures (right). Data are averaged on model vertices
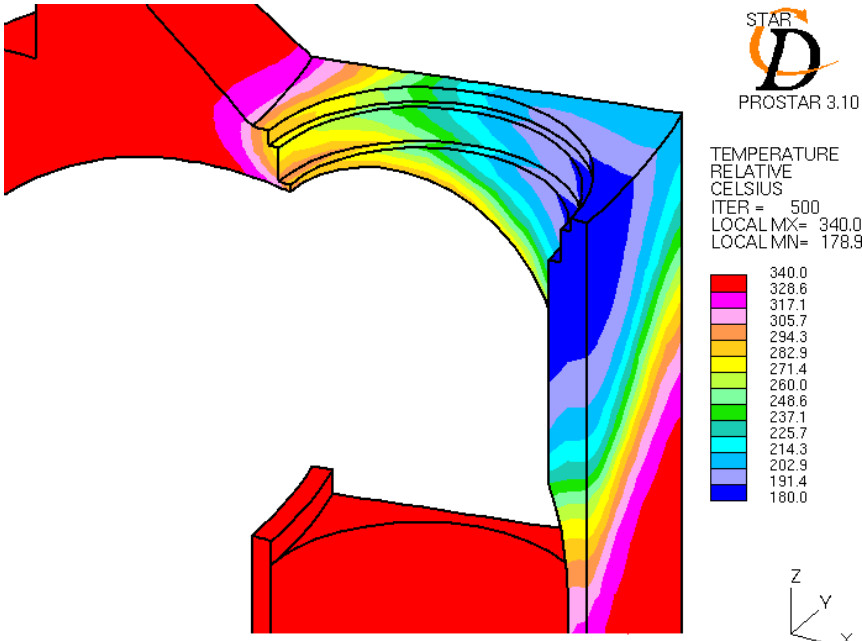
Figure 17 - Case s1: temperature field in the solid structures of the top part of the target. Data are averaged on model vertices.
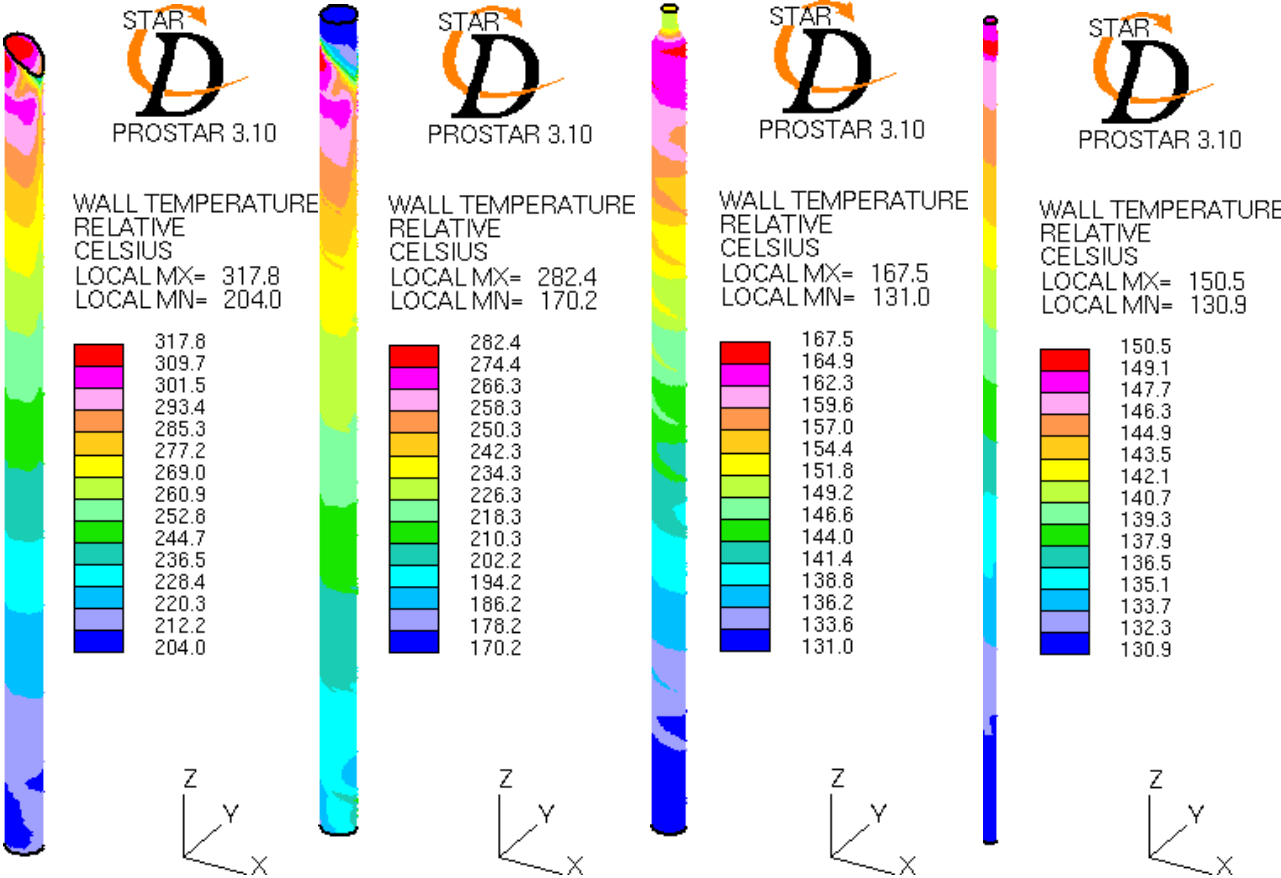
Figure 18 - Case s1: wall temperature fields on (from left to right) the external and internal walls of the pin pipe and of the pin body.
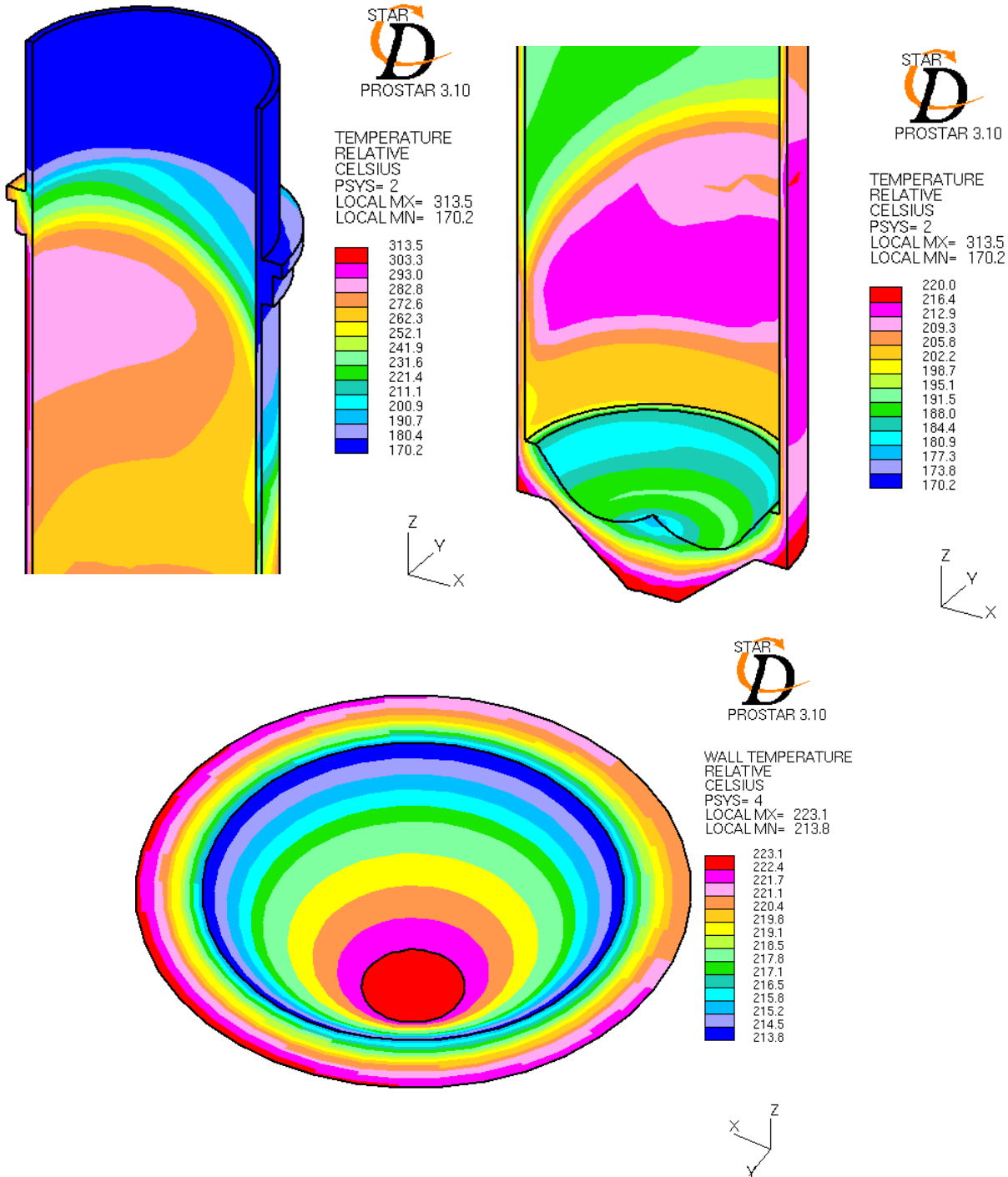
Figure 19 - Case s1: temperature field in the top and bottom part of the pin pipe (top) and on the pin-cap bottom wall (bottom). Data are averaged on model vertices.
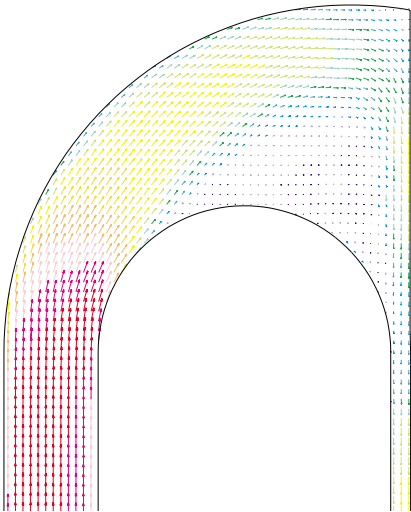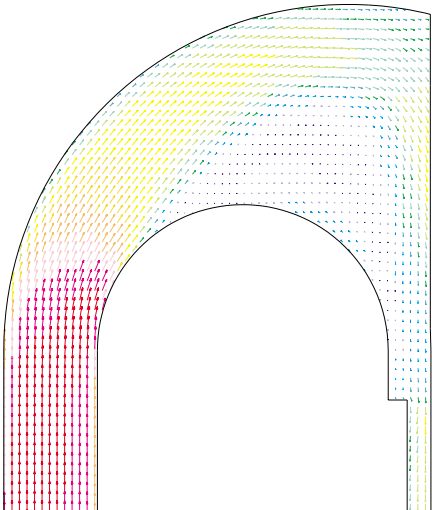
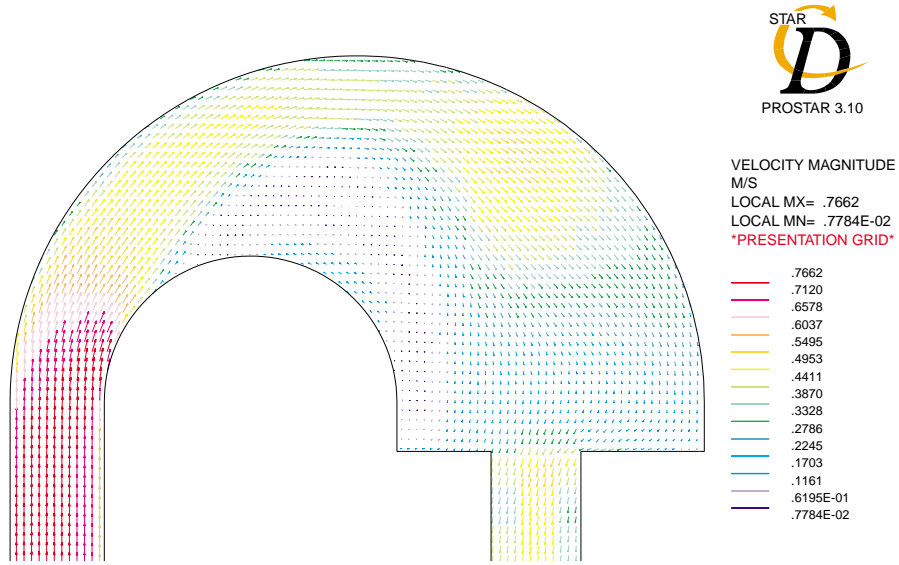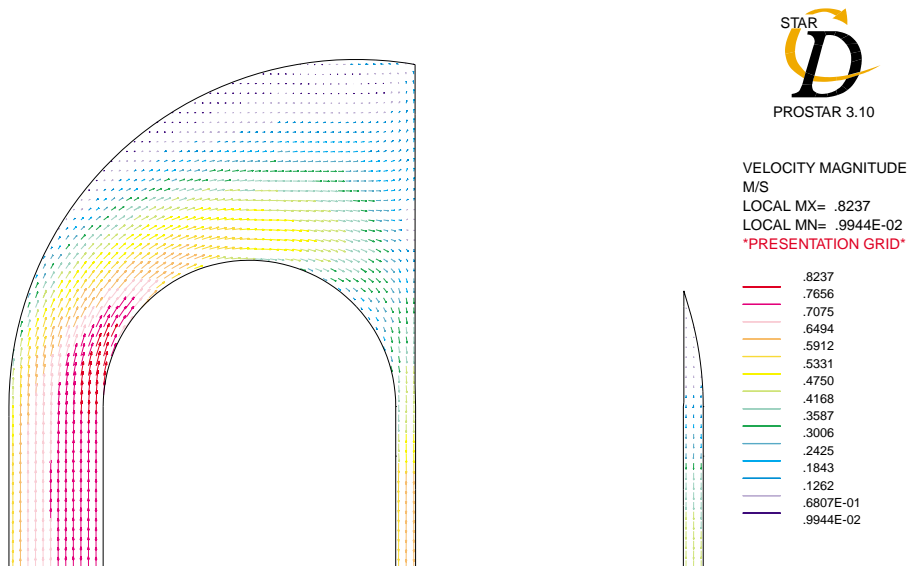Figure 20 - Case s2: PbBi velocity field in various rz sections (system s2) cutting the top part of the target. From top to bottom: θ = 0, 6, 11 deg.
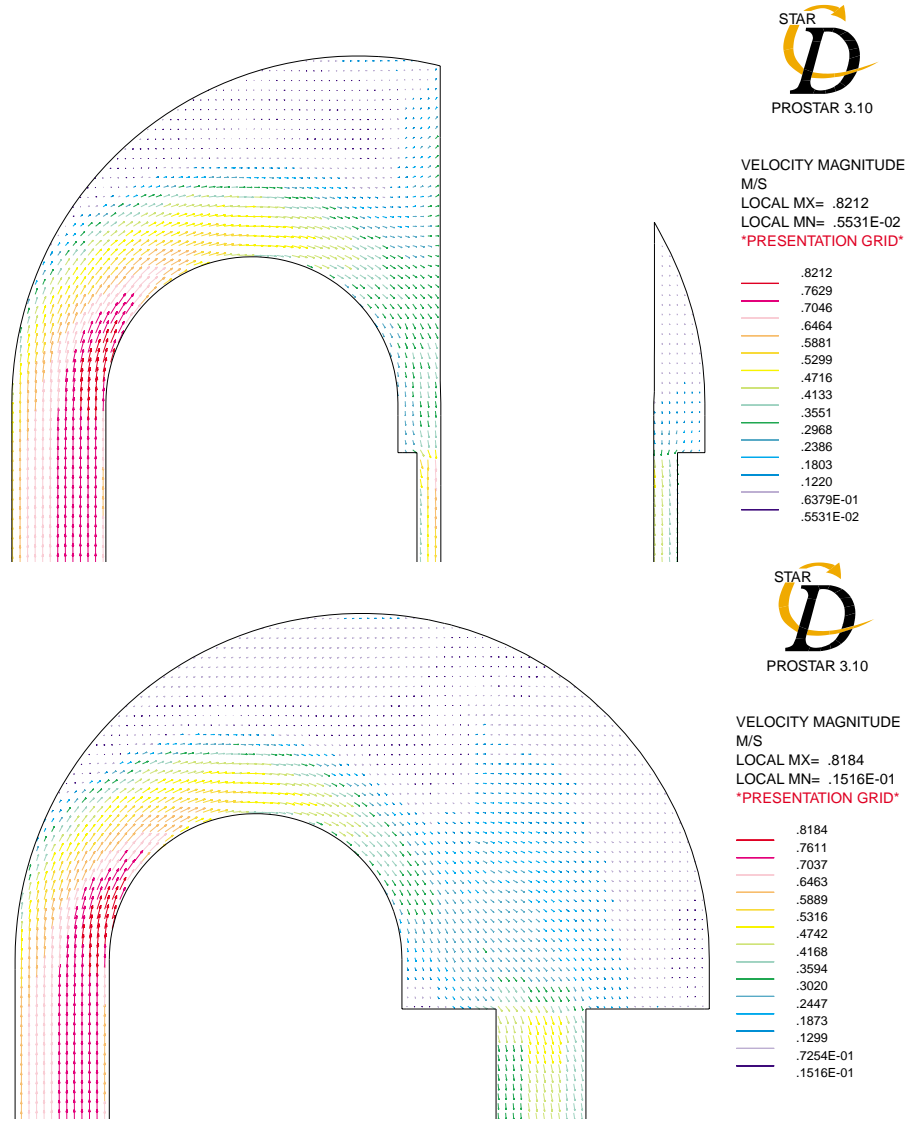
Figure 21 - Case s3: PbBi velocity field in various rz sections (system s2) cutting the top part of the target. From top to bottom: θ = 0, 6, 11 deg.
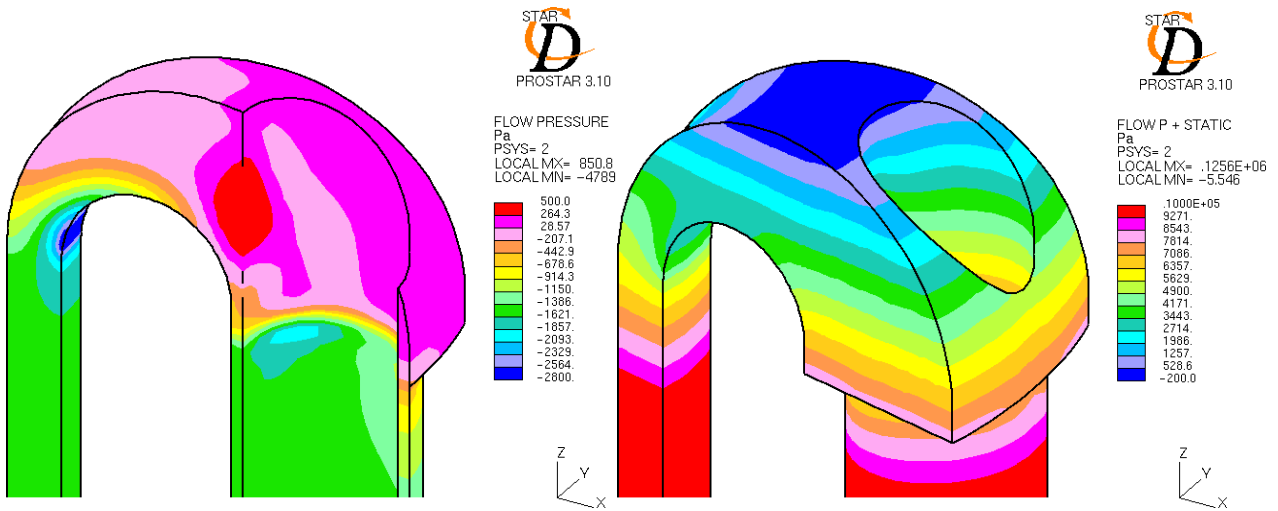
Figure 22 - Case s3: PbBi piezometric (left) and static (right) pressure field in the top part of target.

Figure 23 - Case s3: PbBi temperature field in the top part of the target; full and half model. Data are averaged on model vertices.
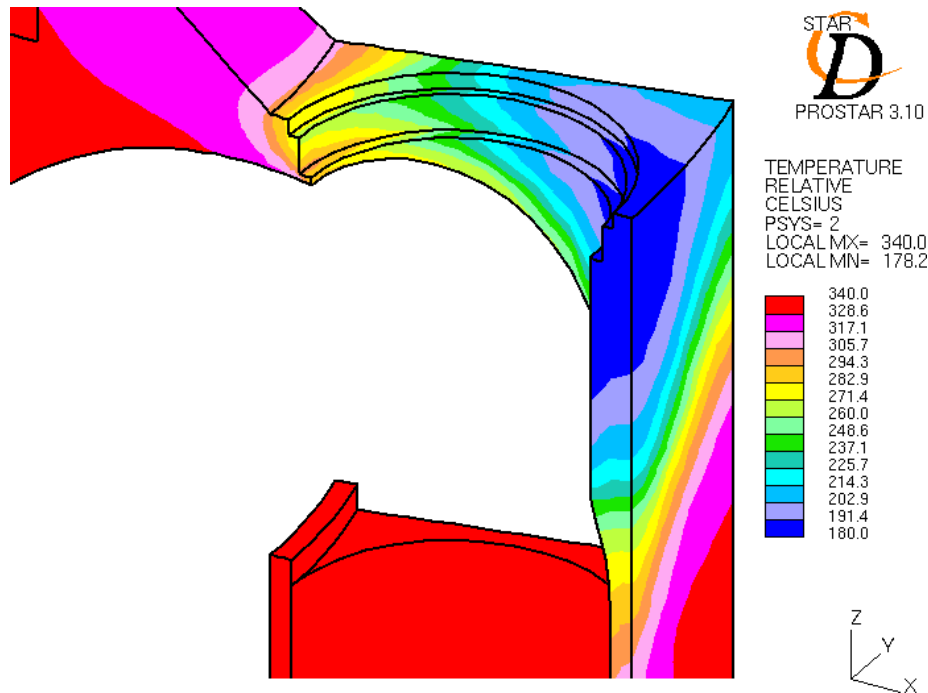
Figure 24 - Case s3: temperature field in the solid structures of the top part of the target. Data are averaged on model vertices.

7   Transient analysis (case t1)

A beam shut-down transient has been simulated by assigning the following time-varying PbBi inlet temperature [5]:

$$T_{in}(t) = T_{in}(0) - T_1 (1 - e^{-at}) - T_2 (1 - e^{-bt})$$

where $T_1 = 80$ °C, $T_2 = 30$ °C, $a = 1$ s^{-1} and $b = 0.04$ s^{-1}. The inlet oil temperature was kept constant.

In order to make the simulation numerically approachable, the velocity fields of both the PbBi and the oil were considered frozen. This implies the assumption that buoyancy effects are negligible during the transient. This is surely true for the oil, and a reasonable assumption in the case of the PbBi. With this approximation, it was possible to use a time step of 2×10^{-3} s, solving only the temperature equation, and resulting in a computational time of about 10 hours running in parallel on 6 IBM SP3 processors.

The time evolution of the following temperatures is plotted in Figure 25

- inlet PbBi temperature;
- outlet PbBi mean temperature;
- outlet oil mean temperature;
- PbBi minimum temperature;
- Oil maximum temperature;

- maximum and minimum temperatures in the upper part of the target solid structures;
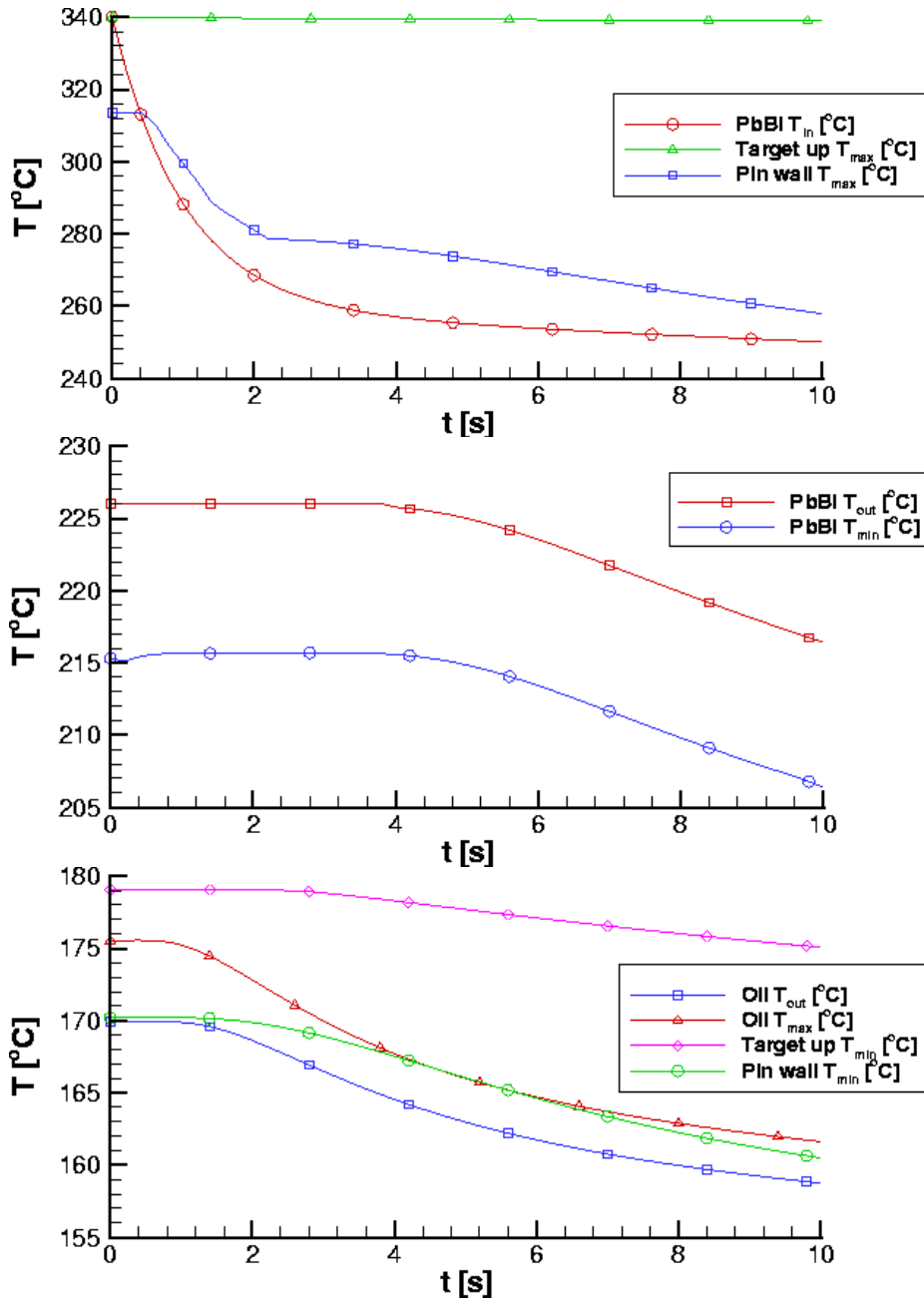- maximum and minimum temperatures in the pin wall.

Figure 25 - Case t1: time variation of the inlet, outlet and minimum PbBi temperatures, of the outlet and maximum oil temperature, and of the minimum and maximum temperatures in the upper target structure and in the pin wall (cell data).

8   Conclusions

The detailed thermal-hydraulic CFD simulation of a sector of the Megapie THX, including one of the twelve cooling pins, has been performed with the Star-CD code in steady-state and transient conditions.

Results showed that the THX is capable of exchanging about 695 kW with a total PbBi flow rate of 4 l/s at 340 $^{\circ}$C and a total oil flow rate of 9.5 l/s at 130 $^{\circ}$C.

The influence of the inlet PbBi velocity profile has been analysed by comparing three different cases, one with uniform profile and two with tilted profile in opposite directions. As expected, the inlet velocity profile has no influence on the global THX performance. Some local effects were observed in the case with higher velocity at higher radius (case s3).

A 10 s transient calculation was carried out, simulating a beam shut-down.

All the temperature field in the solid structures have been passed to ENEA-FIS.MET for the structural analysis of thermal stresses

9   References

[1] Megapie web page: http://megapie.web.psi.ch

[2] S. Buono, L. Maciocco, V. Moreau, L. Sorrentino, *Optimisation of the Pin Cooler design for the Megapie Target using full 3D numerical simulations*, CRS4 Tech. Rep. 02/03, January 2002

[3] S. Cevolani, R. Tinti, *Review of the Liquid Metal Lead-Bismuth Alloy Physical Properties,* ENEA Technical Report DT.SBD.00004.

[4] Accompanying Measure on the Assessment of Computational Fluid Dynamics Codes for Heavy Liquid Metals - ASCHLIM, EU project FIS5-2001-0001.

[5] Personal communication from PSI.

[6]] IDEAS web page: http://www.scdc.com/ideas/index.shtml.

[7] Star-CD, Version 3.15 manual, Computational Dynamics, London, 2001.

[8] AEA Technology plc, *CFX-4.2 Solver*, December 1997.

[9] C. Aragonese, S. Buono, G. Fotia, L. Maciocco, V. Moreau, L. Sorrentino, *Benchmark calculations of Mercury flow experiments performed in Riga for the ESS target design*, CRS4 Tech. Rep. 99/21, November 1999.

[10] C. Aragonese, S. Buono, L. Maciocco, V. Moreau, L. Sorrentino, *CFD Simulation of a Heated Round Jet of Sodium in Forced Flow Regime (TEFLU Benchmark)*, CRS4 Tech. Rep. 00/86, July 2001.

[11] M. Jisha, H.B. Rieke, *Modelling assumptions for turbulent heat transfer*.